



Computational modeling of plastic deformation and shear banding in bulk metallic glasses

Jiahao Cheng^a, Somnath Ghosh^{b,*}

^a Department of Civil Engineering, Johns Hopkins University, United States

^b Departments of Civil and Mechanical Engineering, Johns Hopkins University, Baltimore, MD 21218, United States



ARTICLE INFO

Article history:

Received 10 September 2012

Received in revised form 19 November 2012

Accepted 6 December 2012

Available online 20 January 2013

Keywords:

Bulk metallic glasses

Viscosity

Free volume

Shear band

Plastic deformation

ABAQUS

ABSTRACT

A study of plastic deformation of bulk metallic glasses (BMGs) reveals two modes. At low temperatures high stresses plastic deformation is inhomogeneous, in which case the failure of BMGs is mostly due to the formation of a very thin shear band. Inside this band, the evolving strain is highly localized. At high temperatures and low stresses, plastic deformation is homogeneous and the BMGs exhibit a Newtonian viscosity. It is generally acknowledged that the shear-induced free volume evolution plays an important role in the failure of BMGs under both modes of deformation. In this paper, a free volume-based constitutive model is proposed, which accounts for the transition of inhomogeneous to homogeneous deformation and non-Newtonian to Newtonian viscosity. A time integration algorithm is presented in this paper with a description of its implementation in the commercial code ABAQUS through the user-defined material window UMAT. 2 and 3-Dimensional finite element simulations are performed and the model is validated with results of uniaxial compression and micro-indentation experiments for a wide range of temperatures and strain rates. The simulation results exhibit hydrostatic pressure dependence, and suggest that a mixed-power-strain-rate-dependent free volume creation mode is more effective than the commonly used strain-rate-dependent free volume creation law, when considering large temperature ranges.

© 2012 Elsevier B.V. All rights reserved.

1. Introduction

Metallic glasses are amorphous alloys with superior mechanical properties. They possess disordered microstructures due to rapid quenching of the liquid alloy from a molten state that prevent crystallization. Because of their amorphous structure and lack of long-range ordering, crystal defects such as dislocations and grain boundaries that commonly exist in metallic structures do not occur in metallic glass. This results in their superior mechanical properties such as high yield stress, high strength-to-density ratio, corrosion resistance and high wear resistance. Predominantly researched metallic glasses in the recent years include alloys such as Zr–Ti-based ‘Vitreloy’ and Pb-based materials. These differ from the early classes of Au–Si-based metallic glasses, whose production required a high cooling rate of $\sim 10^5$ – 10^6 K/s and yielded thicknesses in the micron scale. This new class of ‘bulk’ metallic glasses or BMG’s has a high glass forming ability at a low critical cooling rate $\sim 1^\circ$ K/s that enables larger thicknesses in the centimeter scale. This progress has enabled the application of BMG in sporting goods, biomedical equipment structural and MEMS materials.

It is now possible to conduct large-scale experiments such as tension, compression and bending tests at temperatures ranging from room temperature to supercooled temperatures, which were previously impossible due to premature crystallization. Experiments on Vitreloy-1 (the first commercially used BMG) exhibited a transition from Newtonian flow at supercooled temperatures to non-Newtonian flow at room temperatures, as well as transition from homogeneous flow to inhomogeneous localized flow as the strain rate is increased in the vicinity of the glass transition temperature ($T_g = 625$ K) [1]. At both temperature regimes, catastrophic failure is observed due to the formation of shear bands, inside which the strain and strain rate highly localized. Development of effective 3D constitutive models for implementation in finite deformation, computer simulation codes is necessary in understanding the shear band formation in bulk metallic glasses.

Considerable efforts have gone into the deformation modeling of BMG. Early work on the atomic and microstructural scales of BMG, e.g. in [2,3] focused on flow defect models, viz. the evolution of free volume, which is considered as the primary mechanism of deformation localization in amorphous structure. However most of these models were one-dimensional, which were not capable of capturing three-dimensional stress and strain states leading to localization and shear banding. A 3D phenomenological finite deformation constitutive model with von-Mises

* Corresponding author. Tel.: +1 410 516 7833; fax: +1 410 516 7473.

E-mail address: sghosh20@jhu.edu (S. Ghosh).

yield criterion and free volume dependent visco-plasticity was developed in [4]. While other studies, e.g. in [5,6] have produced similar models, the model in [4] has the advantage of capturing deformation features over a wide range of temperatures from room temperature to super-liquid region and reproduces experimentally observed stress–strain responses for many different strain-rates. However, the lack of a clear free volume evolution law in [4] impedes its accuracy near the glass transition temperature for certain strain rates. Furthermore, indentation experiments at different scales have shown that the von-Mises criteria is inappropriate in describing the deformation of BMG. AFM images of pyramidal nano-indented surfaces have been compared with simulated values using the Mohr–Coulomb stress criterion in [7], which showed good agreement of the nano-indentation behavior of Vitreloy-1. Spherical micro-indentation tests of Vitreloy-1 have suggested good agreement with values for the Mohr–Coulomb friction parameter are in the range from 0.08 to 0.14 [8]. These agreements are further consolidated in studies of the fracture mechanics, highlighting the effects of hydrostatic pressure in predicting the orientation of fracture surface [9]. Recent studies in [10] suggest that under low stress conditions corresponding to homogeneous deformation, the disordering process of free volume tends to follow a power-law stress–strain-rate behavior. This disordering process in homogeneous deformation modes is found to be strongly correlated to the drop in stress carrying capacity under different strain-rates. Homogeneous deformation modes enables determination of the functional dependencies on stress, strain and strain rate.

The present study extends the above constitutive models for predicting deformation induced shear-band localization in bulk metallic glasses. The constitutive framework incorporates finite deformation kinematics, the Mohr–Coulomb yield criteria and the kinetic law governing the evolution of density and free volume under different strain rates. The power law disordering model for free volumes is extended to a moderately high stress region. Numerical algorithms are developed for implementation of this model into the commercial software ABAQUS through a user-defined material subroutine UMAT. The model is validated with results of uniaxial compression and micro-indentation tests for a range of temperatures and strain-rates.

2. Constitutive model for BMG

A finite deformation, elastic-viscoplasticity model is developed in this section for accommodating large deformation within shear bands. The formulation follows the multiplicative decomposition, logarithmic strain measures and exponential mapping proposed in [11,12], which has been proved to be efficient and accurate for large strain elasto-plasticity without loss of generality. The inelastic part of the deformation is described using the Mohr–Coulomb yield criteria with a thermodynamically-based associated flow rule and free-volume dependent isotropic hardening/softening law.

2.1. Kinematic relations and increments

The kinematic model assumes a multiplicative decomposition of the deformation gradient into elastic and plastic parts, with the establishment of an intermediate configuration as:

$$\mathbf{F} = \mathbf{F}^e \mathbf{F}^p, \quad \det \mathbf{F}^e > 0 \quad (1)$$

where the \mathbf{F}^e and \mathbf{F}^p are the elastic and plastic components of the deformation gradient tensor respectively. The plastic velocity gradient pull-back to intermediate configuration is expressed as:

$$\dot{\mathbf{L}}^p = \dot{\mathbf{F}}^p \mathbf{F}^{p-1} \quad (2)$$

The symmetric part of \mathbf{L}^p is the plastic deformation rate tensor \mathbf{D}^p , while the skew part $\mathbf{W}^p = \text{asym}(\mathbf{L}^p)$ describes the plastic spin in the intermediate configuration.

In the present BMG constitutive model, plastic deformation is assumed to be dominated by free volume that causes volumetric change without any plastic spin. Vanishing plastic spin is considered in this model according to [4,5], and consequently:

$$\mathbf{L}^p \simeq \text{sym}(\mathbf{L}^p) = \mathbf{D}^p \quad (3)$$

Integrating Eq. (2) from time t to $t + \Delta t$ by the backward Euler algorithm and substituting Eq. (3), yields an exponential update of plastic deformation gradient tensor [12] as:

$$\mathbf{F}_0^{t+\Delta t} \mathbf{F}^p = \exp(\Delta t \mathbf{F}_0^{t+\Delta t} \mathbf{D}^p) \mathbf{F}_0^p \quad (4)$$

The superscripts t to $t + \Delta t$ corresponds to the current configuration, while the subscript 0 corresponds to the reference configuration. Additionally, the logarithmic elastic strain tensor is defined as (see [12]):

$$\mathbf{E}^e = \frac{1}{2} \ln(\mathbf{F}^e \mathbf{F}^e) \quad (5)$$

This has the advantage of effectively reducing the finite strain update to the infinitesimal strain update, expressed as:

$$\mathbf{F}_0^{t+\Delta t} \mathbf{F}^e = \mathbf{F}_0^{t+\Delta t} \mathbf{F}_0^t \mathbf{F}^{eT} \exp(-\Delta t \mathbf{F}_0^{t+\Delta t} \mathbf{D}^p) = \mathbf{F}_t^{t+\Delta t} \mathbf{F}_*^e \exp(-\Delta t \mathbf{F}_*^e \mathbf{D}^p)$$

where

$$\mathbf{F}_t^{t+\Delta t} \mathbf{F}_*^e \triangleq \mathbf{F}_0^{t+\Delta t} \mathbf{F}_0^t \mathbf{F}^{eT} \quad (6)$$

If $\mathbf{F}_*^e = \frac{1}{2} \ln(\mathbf{F}_t^{t+\Delta t} \mathbf{F}_*^e \mathbf{F}_*^e)$ represents a trial elastic logarithmic strain tensor, the logarithmic elastic strain at time $t + \Delta t$ may be expressed as:

$$\mathbf{F}_0^{t+\Delta t} \mathbf{E}^e \simeq \mathbf{E}_*^e - \Delta t \mathbf{F}_*^e \mathbf{D}^p \quad (7)$$

2.2. Hyperelastic stored energy function and stress–strain relation

For an isotropic BMG response, a hyperelastic stored energy function is defined in terms of the logarithmic elastic strain tensor as:

$$\psi^e = \mu \|\mathbf{E}^{e,dev}\|^2 + \frac{k}{2} \{tr(\mathbf{E}^e) - \alpha_t(T - T_0)\}^2 \quad (8)$$

where μ and k are the shear and bulk modulus respectively, $tr(\mathbf{E}^e)$ is a measure of volume change produced by the hydrostatic stress, and $\mathbf{E}^{e,dev} = \mathbf{E}^e - \frac{1}{3} tr(\mathbf{E}^e) \mathbf{I}$ is the deviatoric part of elastic logarithmic strain. $\alpha_t(T - T_0)$ is the volumetric strain due to change in temperature T , where α_t is the coefficient of thermal expansion and T_0 is the initial temperature.

The free energy is defined as the sum of the hyperelastic stored energy and the thermal energy as:

$$\psi = \psi^e(\mathbf{E}^e, T) + \psi^T(T) \quad (9)$$

where the thermal energy is:

$$\psi^T = \rho_0 C_v \left\{ (T - T_0) - T \log \frac{T}{T_0} \right\} \quad (10)$$

In this expression, ρ_0 is the mass density per unit volume in reference configuration and C_v is the mass specific heat at the constant volume.

The stress–strain relation for BMG materials has been expressed in terms of the Mandel stress tensor Ξ [4]. The symmetric part of this stress tensor is related to the second Piola–Kirchhoff stress tensor \mathbf{S} and Kirchhoff stress tensor $\boldsymbol{\tau}$ as (see [12]):

$$\Xi_{sym} = \frac{1}{2}(\mathbf{C}^e \mathbf{S} + \mathbf{S} \mathbf{C}^e) = \mathbf{U}^e \mathbf{S} \mathbf{U}^e = \mathbf{R}^{eT} \boldsymbol{\tau} \mathbf{R}^e = \bar{\boldsymbol{\tau}} \quad (11)$$

$\mathbf{U}^e = \mathbf{U}^{Te}$ is the elastic right stretch tensor of the elastic deformation gradient, obtained by polar decomposition of $\mathbf{F}^e = \mathbf{R}^e \mathbf{U}^e$, where \mathbf{R}^e is the orthogonal rotation tensor. For isotropic elasticity, the right Cauchy–Green tensor \mathbf{C}^e has the same eigenvector as the second Piola–Kirchhoff stress tensor \mathbf{S} and thus they can commute as in the second term of Eq. (11). $\bar{\boldsymbol{\tau}}$ corresponds to a rotated Kirchhoff stress tensor in an intermediate rotated configuration that can be derived from the hyperelastic stored energy [12,13] as:

$$\bar{\boldsymbol{\tau}} = \frac{\partial \psi}{\partial \mathbf{E}^e} \quad (12)$$

Inserting Eqs. (8) and (12) in Eq. (11) yields the explicit form of Mandel stress as:

$$\Xi_{sym} = \frac{\partial \psi}{\partial \mathbf{C}^e} = 2\mu \mathbf{E}^{e,dev} + k [\text{tr}(\mathbf{E}^e) - \alpha_t(T - T_0)] \mathbf{I} \quad (13)$$

This stress is used as the thermodynamic stress measure in the subsequent constitutive model.

2.3. Yield surface and associated flow rule

Thermodynamic conditions of extremum dissipation in terms of the generalized yield function $f(\Xi_{sym}, \boldsymbol{\beta}, \sigma_f)$, yields the flow rule and other evolutionary plasticity relations for internal variables as [12]:

$$\mathbf{D}^p = \dot{\lambda} \frac{\partial f}{\partial \Xi_{sym}} \quad (14)$$

$$\dot{\xi} = -\dot{\lambda} \frac{\partial f}{\partial \boldsymbol{\beta}} \quad (15)$$

$$\dot{\zeta} = -\dot{\lambda} \frac{\partial f}{\partial \sigma_f} \quad (16)$$

In these equations, the yield function $f = f(\Xi_{sym}, \boldsymbol{\beta}, \sigma_f)$ is assumed to be a function of the stress tensor Ξ , a back-stress tensor $\boldsymbol{\beta}$ and a scalar flow stress. ξ is a tensor internal variable resembling a strain-rate that is work-conjugate to $\boldsymbol{\beta}$, and ζ is a scalar internal variable resembling strain that is work-conjugate to the flow stress σ_f . The consistency parameter $\dot{\lambda}$ appears in all the three relations (14)–(16). This can be briefly illustrated from the solution of the maximum plastic dissipation condition [12]:

$$\mathbf{D}^p = \boldsymbol{\beta} : \dot{\xi} + \sigma_f \dot{\zeta} + \Xi_{sym} : \mathbf{D}^p \geq 0$$

with the yield function f as a constraint. By extremizing the Lagrangian, in which $\dot{\lambda}$ is the Lagrange multiplier, given as:

$$L(\Xi_{sym}, \boldsymbol{\beta}, \sigma_f) = \mathbf{D}^p - \dot{\lambda} f$$

the extreme condition yields Eqs. (14)–(16) with the consistency parameter $\dot{\lambda}$. The back-stress term is associated with kinematic hardening that arises in cyclic loading and is not considered further in this work. Uniaxial compression and tension tests in [9] have shown that hydrostatic component of stress has a significant effect on the yield function, representing plastic deformation in BMG. The hydrostatic stress dependent yield function has a direct effect on the orientation of shear band formation [14], that is also corroborated through indentation experiments in [15]. The pressure-sensitive yield function is constructed following the Mohr–Coulomb framework as:

$$f = \tau + a \bar{p} - \sigma_f \quad (17)$$

where $\tau = \sqrt{\left(\Xi_{sym}^{dev}\right)^{dev} : \left(\Xi_{sym}^{dev}\right)^{dev}}$ is proportional to the effective Von-Mises stress, $\bar{p} = \frac{1}{3} \text{tr}(\Xi_{sym})$ is the hydrostatic pressure, a is a pressure sensitivity parameter and σ_f is a rate-dependent, isotropic hardening flow stress.

The plastic rate of deformation tensor \mathbf{D}^p is expressed in terms of the flow direction tensor \mathbf{N}^{flow} , which is derived from (17) as:

$$\mathbf{D}^p = \dot{\epsilon}^p \mathbf{N}^{flow} \text{ where } \mathbf{N}^{flow} = \frac{\partial f}{\partial \Xi_{sym}} = \frac{1}{3} a \mathbf{I} + \mathbf{M} \quad (18)$$

$\dot{\epsilon}^p$ is a plastic flow multiplier that may be equated to the consistency parameter $\dot{\lambda}$ in Eq. (14). The tensor \mathbf{M} is the direction corresponding to the effective shear stress [4,16], i.e.

$$\mathbf{M} = \frac{\partial \tau}{\partial \Xi_{sym}} \text{ s.t. } \text{tr}(\mathbf{M}) = 0 \text{ and } \mathbf{M}^T = \mathbf{M} \quad (19)$$

Substituting Eq. (13) into Eq. (19) yields:

$$\mathbf{M} = \frac{\mathbf{E}^{e,dev}}{\|\mathbf{E}^{e,dev}\|} \quad (20)$$

This is consistent with other BMG models, such as in [16]. Correspondingly, the plastic rate of deformation tensor is given as:

$$\mathbf{D}^p = \dot{\epsilon}^p \left(\frac{1}{3} a \mathbf{I} + \mathbf{M} \right) \quad (21)$$

Also from (16) and (17), the rate of the internal scalar variable may be related as $\dot{\zeta} = \dot{\lambda} = \dot{\epsilon}^p$. Hence $\dot{\epsilon}^p$ is the only internal variable in the model.

Eq. (18) shows that plastic incompressibility constraint does not apply to the BMG constitutive model. Plastic volumetric change is caused by free volume change, which governs the plastic deformation. The free volume of an atom is the nearest neighboring free space, whose size (atomic hard-sphere) is greater than a critical volume v^* . The average free-volume is defined as the free volume in the atomic configuration v_f , in relation to the critical volume v^* per atom in a unit volume, i.e. the free volume concentration is expressed as:

$$\xi = \frac{v_f}{v^*} \quad (22)$$

In Section 2.5 it will be shown that the free-volume evolution law has a form:

$$\dot{\xi} = k^+ \tau \dot{\epsilon}^p + k^- \dot{\epsilon}^p \quad (23)$$

where ξ is the free-volume concentration. The first term on the right hand side is the shear induced free-volume nucleation, while the second term is the free-volume annihilation due to structure relaxation. Since $\dot{\epsilon}^p = \frac{\dot{\xi}}{k^+ \tau + k^-}$ from Eq. (23), the dilatation part of the plastic rate of deformation \mathbf{D}^p in Eq. (21) can be expressed as:

$$\frac{1}{3} a \dot{\epsilon}^p \mathbf{I} = \frac{1}{3} \frac{a}{k^+ \tau + k^-} \dot{\xi} \mathbf{I} \quad (24)$$

Eq. (24) shows the explicit connection between the plastic rate of dilatation and the free-volume evolution, which has also been shown in the model of [5].

2.4. Flow stress

The flow stress σ_f , which exhibits strain hardening, thermal softening, as well as rate-dependence, is expressed as:

$$\sigma_f = \sigma_0 + \eta \dot{\epsilon}^p \quad (25)$$

Here σ_0 is a threshold stress that determines the onset of inelastic deformation under different applied strain rates. The viscosity parameter $\eta = \eta(\xi, T, \dot{\epsilon})$ is a function of free-volume, temperature and strain rate. Its specific form may be derived from thermodynamic considerations. Based on the free-volume theory in [2], plastic deformation in metallic glasses occurs by the shear of localized groups of atoms, for which the flow equations under an external shear stress τ is:

$$\dot{\gamma} = 2f_0 \exp\left(-\frac{\alpha}{\xi}\right) k_f \sinh\left(\frac{\tau\Omega}{2k_B T}\right) \quad (26)$$

where $\dot{\gamma}$ is the shear strain rate, f_0 is frequency of atomic vibration, $\alpha(\leq 1)$ is a geometrical factor, k_f is a temperature-dependent constant, Ω is the atomic volume and k_B is the Boltzmann constant. At low stresses and high temperatures, the hyperbolic term in of Eq. (26) approximates a linear form. Under these conditions, the Eq. (26) is assumed to describe the visco-plastic response of BMG. Hence $\dot{\gamma}$ and τ may be replaced by $\dot{\epsilon}^p$ and σ_f for which Eq. (26) reduces to:

$$\dot{\epsilon}^p = 2f_0 \exp\left(-\frac{\alpha}{\xi}\right) k_f \frac{\Omega}{2k_B T} \sigma_f \quad (27)$$

The inverse kinetic relation is then established as:

$$\sigma_f = \frac{k_B T}{f_0 \Omega} \frac{1}{k_f} f_0 \exp\left(\frac{\alpha}{\xi}\right) \dot{\epsilon}^p = \eta_0(T) \exp\left(\frac{\alpha}{\xi}\right) \dot{\epsilon}^p = \eta(\xi, T) \dot{\epsilon}^p \quad (28)$$

Eq. (28) is the flow equation with the Newtonian viscosity as $\eta_0 \exp\left(\frac{\alpha}{\xi}\right)$ in the low stress and high temperature regime. In [17], η_0 has been alternatively described by an entropy-based phenomenological model as $\frac{h}{v}$, where h is the Planck's constant.

In the high stress and low temperature regime, metallic glasses are often observed to have non-Newtonian viscosity and inhomogeneous flow. A transition from Newtonian to non-Newtonian viscosity has been experimentally observed in [18] with decrease in temperature and increase in strain-rate. To extend Eq. (28) to a broader range of temperatures and strain-rates, a general expression of viscosity has been proposed in [17] as:

$$\eta(\xi, T, \dot{\epsilon}) = \frac{\eta_0}{1 + \exp\left(\frac{\alpha}{\xi}\right) \left(\frac{\eta_0 \dot{\epsilon}}{\sigma_0}\right)^{b(T)}} \exp\left(\frac{\alpha}{\xi}\right) \quad (29)$$

where σ_0 is a reference stress. The term $\exp\left(\frac{\alpha}{\xi}\right) \left(\frac{\eta_0 \dot{\epsilon}}{\sigma_0}\right)^{b(T)}$ account for the temperature and strain-rate effects. The temperature dependent coefficient has been proposed to be $b(T) = 1.0 - 4.325 \times 10^{-10} \times (T - 293)^3$ in [4]. While this expression is suitable for lower strain-rates, the accuracy drops for rates higher than 10^{-2} . Consequently, a third-order polynomial expression in temperature is fitted from the experimental results in [4] as $b(T) = 0.995 - 9.15 \times 10^{-5} T + 2.6 \times 10^{-7} T^2 - 1.992 \times 10^{-10} T^3$ where T is in K. In the temperature range 293–700 K, the value of $b(T)$ is between 1.0 and 0.95, which corresponds to a non-Newtonian viscosity. At high temperatures the term $\exp\left(\frac{\alpha}{\xi}\right) \left(\frac{\eta_0 \dot{\epsilon}}{\sigma_0}\right)^{b(T)} \rightarrow 0$ and hence the Newtonian viscosity is recovered. Values of these parameters are listed

Table 1
Mechanical properties and parameters for Vitreloy-1 (Data is taken from [4]).

Property	Value
Young's modulus in glassy state E_{gl}	70 GPa
Young's modulus in supercooled liquid state E_{sc}	23.5 GPa
Slope of Young's modulus in glassy state k_{Egl}	−80 MPa/K
Slope of Young's modulus in supercooled liquid state k_{Esc}	0 MPa/K
Parameter for the Young's modulus ΔE	24.63
Poisson's ratio ν	0.36
Reference stress σ_0	0.54 GPa
Mass density (room temperature) ρ	6000 kg m ^{−3}
Melting temperature T_m	936 K
Glass transition temperature T_g	625 K
Reference temperature for $\xi_T: T_{ref}$	693 K
Parameter for threshold stress b	1
"Gas" limit viscosity τ_0	4×10^{-5} Pa s
Material parameter for $\dot{\xi}: \chi$	0.4
Material parameter for $\dot{\xi}: \alpha'_x$	0.4
Parameter for viscosity: α	0.11
Parameter in the Cohen–Grest model: d1	47,948
Parameter in the Cohen–Grest model: d2	189
Thermal expansion coefficient α_T	4.0×10^{-5} K ^{−1}

in Table 1. The viscosity is Eq. (29) is very sensitive to free-volume concentration ξ . The conventional viscosity form is obtained by replacing the viscosity term in Eq. (28) with Eq. (29) and adding a threshold term, i.e.

$$\sigma_f = \sigma_0 + \eta(\xi, T, \dot{\epsilon}) \dot{\epsilon}^p \quad (30)$$

The threshold stress σ_0 is the experimentally observed elastic limit and varies with temperature and strain-rates. In this model, it is taken as an average of the steady state flow stress as:

$$\sigma_0 = b\eta(\xi, T, \dot{\epsilon}) \dot{\epsilon} \quad (31)$$

where b is a material constant and $\dot{\epsilon} = \|\text{sym}(\dot{\mathbf{F}}\mathbf{F}^{-1})\|$ is the total effective strain rate. Eqs. (29)–(31) define the hardening and softening response in this model.

2.5. Free-volume and temperature evolution

The evolution of free-volume that occurs during shearing in plastic deformation is regarded as an order–disorder process. The kinetic law of free-volume generally incorporates a combination form of creation and annihilation in the form:

$$\dot{\xi} = \chi(\dot{\xi}^+ + \dot{\xi}^-) \quad (32)$$

where χ is an order constant. While diffusion also contributes to the change of free-volume, it is not considered in this mode due to the lack of understanding of this process. Free-volume is created in shear mode when an atom is squeezed into a void, which is smaller than the critical volume. The resulting expression for free-volume creation is given in [2] as:

$$\dot{\xi}^+ = \frac{2\alpha f_0}{v_f S} \exp\left(-\frac{\alpha}{\xi}\right) k_f \frac{k_B T}{S} \left[\cosh\left(\frac{\tau\Omega}{2k_B T}\right) - 1 \right] \quad (33)$$

The bracketed term in Eq. (33) can be expanded in a Taylor series as

$$\cosh\left(\frac{\tau\Omega}{2k_B T}\right) - 1 = 1 + \frac{1}{2} \left(\frac{\tau\Omega}{2k_B T}\right)^2 + \dots - 1 \quad (34)$$

For low stresses and high temperatures, the higher order terms in the series can be ignored to yield the functional form:

$$\dot{\xi}^+ = \frac{\alpha f_0}{v_f S} \exp\left(-\frac{\alpha}{\xi}\right) k_f \frac{\tau^2 \Omega^2}{2k_B T} \quad (35)$$

Substituting Eq. (26) into (35) and replacing τ with σ_f yields the relation for work-rate (power) dependent free-volume creation as [10]:

$$\dot{\xi}_f^+ = \frac{1}{2} \frac{\alpha \Omega}{v_f S} \sigma_f \dot{\epsilon}^p = a'_x \alpha \sigma_f \dot{\epsilon}^p \quad (36)$$

Disordering is described by the single adjustable parameter a'_x . In [10], the evolution law in Eq. (36) has been shown to accurately predict the uniaxial compression creep experimental response of Pb-based metallic glass up to moderately high stresses and temperatures (600 MPa, 550 K). For higher stress regimes, the free-volume evolution law follows a strain-rate-dependent form as given in [19,45]. The hyperbolic functions in Eqs. (26) and (33) approximate exponentials and consequently, Eq. (33) reduces to:

$$\dot{\xi}_f^+ = a_x \alpha \dot{\epsilon}^p \quad (37)$$

where a_x is a temperature and strain-rate dependent parameter. Combining Eqs. (36) and (37), a general form of the free-volume evolution for a wide range of stresses and temperatures regions may be given as:

$$\dot{\xi}_f^+ = a_x^c (a'_x \sigma_f)^{1-c} \alpha \dot{\epsilon}^p \quad (38)$$

where a'_x is a constant and the parameter $c(\frac{\sigma_f}{T}) \in [0, 1]$ accounts for the transition from the low stress regime to the high stress regime. a'_x has been computed in [4] and the parameters c has been fitted to experimental data in [1] to yield $c = 0.5 \left[1 + \tanh \left(10^{-5} \left(\frac{\sigma_f}{T} - 0.7 \times 10^6 \right) \right) \right]$.

Annihilation of the free-volume takes place by bimolecular process induced structure relaxation [10], where it is assumed that the excess free volume created by shear will tend to be relaxed toward a metastable equilibrium value ξ_T . Using a simple model for visco-elastic behavior of Newtonian flows, the relaxation time is related to the viscosity as $t = \frac{\eta}{\mu}$, and the free volume relaxation rate is [4]:

$$\dot{\xi} = \frac{\xi - \xi_T}{\eta/\mu} = \frac{\xi - \xi_T}{\sigma_f/\mu \dot{\epsilon}^p} \quad (39)$$

The equilibrated, temperature dependent free-volume concentration, which represents the free-volume in a stress-free state according to the Cohen-Grest or CG model [20] is given as:

$$\xi_T = \frac{1}{2d_1} \left[T - T_{ref} + \sqrt{(T - T_{ref})^2 + d_2 T} \right] \quad (40)$$

This parameter ξ_T may also be used as the initial value of the free-volume concentration. For monotonic loading case starting from a stress-free state, the free-volume concentration evolution rate should always be larger or equal than zero in the presence of a positive plastic strain rate, i.e. $\dot{\xi} \geq 0 \forall \dot{\epsilon}^p \geq 0$.

The free-volume concentration ξ_T is determined by the equilibrium temperature according to the Cohen-Grest or CG model [20], which also affects the viscosity. Additionally, experimental measurements of the elastic modulus of the a variety of bulk metallic glasses, e.g. in [21,22] have shown a dependence on temperature. The shear modulus, bulk modulus and Poisson's ratio have been measured at temperatures ranging from 400 K down to liquid nitrogen temperature for Zr, ZrCu and Mg-based BMG's in [23]. These studies have shown low Poisson's ratio and high shear and bulk moduli at low temperatures, which are consistent with experimental observations in [21]. A functional form of the temperature dependent Young's modulus $E(T)$ is assumed following the model in [24] for amorphous polymers as:

$$E(T) = \frac{1}{2}(E_{gl} + E_{sc}) - \frac{1}{2}(E_{gl} - E_{sc}) \tanh \left(\frac{1}{\Delta_E} (T - T_g) \right) + k_E (T - T_g) \quad (41)$$

where E_{gl}, E_{sc} are the moduli in glassy and supercooled liquid regions respectively, Δ_E is a fitting parameter, T_g is the glass transition temperature and k_E corresponds to the slope of temperature variation of the Young's modulus beyond the transition region, i.e.

$$k_E = \begin{cases} k_{Egl} & \text{if } T < T_g \\ k_{Esc} & \text{if } T \geq T_g \end{cases} \quad (42)$$

In the case of inhomogeneous deformation, temperature evolution is generally due to adiabatic heating inside the very thin shear band where the shear strain rate is much higher than in other parts. This rate of temperature change can be equated to the conventional heat flux and plastic energy dissipation terms as [4]:

$$\rho_0 C_v \dot{T} = \beta_0 \sigma \dot{\epsilon}^p - \nabla \cdot \mathbf{H} \quad (43)$$

where β_0 is the Taylor–Quinney coefficient, \mathbf{H} is the outward heat flux. For isothermal and adiabatic heating condition the $\dot{T} = 0$ and $\nabla \cdot \mathbf{H} = 0$ respectively. Constitutive parameters for the Vitreloy-1 BMG is given in Table 1.

3. Implementation of the constitutive model in the commercial code ABAQUS

The constitutive model discussed in Section 2 is incorporated in the commercial FEM code ABAQUS through the user interface material subroutine (UMAT). An implicit time integration scheme with the return mapping algorithm [25] is used in UMAT to update stress, effective plastic strain rate, free volume, temperature and other state dependent variables from a known state at time t to next incremental state at time $t + \Delta t$. The following general steps are pursued to integrate the constitutive relations. This is also depicted in Fig. 1.

- (1) Start with the elastic predictor corresponding to $\Delta \epsilon^p = 0$, that is assuming an elastic increment. Thus:

$$\mathbf{F}_{t+\Delta t}^{p,pre} = \mathbf{F}_t^p, \mathbf{F}_{t+\Delta t}^{e,pre} = \mathbf{F}_{t+\Delta t} \mathbf{F}_{t+\Delta t}^{p-1} \quad (44)$$

Calculate $\psi_{t+\Delta t}, \tau_{t+\Delta t}, \bar{p}_{t+\Delta t}, \sigma_{f(t+\Delta t)}$ and other terms based on this decomposition.

- (2) Determine: $\tau_{t+\Delta t} + a\bar{p}_{t+\Delta t} - \sigma_{f,t+\Delta t}$
 - (i) If $\tau_{t+\Delta t} + a\bar{p}_{t+\Delta t} - \sigma_{f,t+\Delta t} \leq 0$, then the increment is elastic. $\Delta \epsilon^p = 0$ and the corresponding results are correct. The elastic updates correspond to the total updates.
 - (ii) If $\tau_{t+\Delta t} + a\bar{p}_{t+\Delta t} - \sigma_{f,t+\Delta t} > 0$, then the increment is inelastic. Introduce the corrector using a Newton–Raphson iterative update.
- (3) Calculate $\Delta \epsilon^p$ using a Newton–Raphson iterative scheme

$$\Delta \epsilon^{p(i+1)} = \Delta \epsilon^{p(i)} - \frac{H(\Delta \epsilon^{p(i)})}{\frac{H(\Delta \epsilon^p + \delta \epsilon^p) - H(\Delta \epsilon^{p(i)} - \delta \epsilon^p)}{2\delta \epsilon^p}} \quad (45)$$

where $H(\Delta \epsilon^p) = \tau_{t+\Delta t} + a\bar{p}_{t+\Delta t} - \sigma_{f(t+\Delta t)}$ and $\delta \epsilon^p$ corresponds to a perturbation on $\Delta \epsilon^p$.

- (4) Calculate the free-volume concentration increment $\Delta \xi$ from Eq. (31). The decomposition of deformation gradient is now altered as:

$$\mathbf{F}_{t+\Delta t}^p = \exp(a'\Delta \xi \mathbf{I} + \Delta \epsilon^p \mathbf{M}_{t+\Delta t}) \mathbf{F}_t^p, \mathbf{F}_{t+\Delta t}^e = \mathbf{F}_{t+\Delta t} \mathbf{F}_{t+\Delta t}^{p-1} \quad (46)$$

where the plastic flow direction tensor $\mathbf{M}_{t+\Delta t}$ is calculated explicitly from Eq. (19) and the predictor: $\mathbf{F}_{t+\Delta t}^{e,pre}$.

- (5) Repeat calculation for $\psi_{t+\Delta t}, \tau_{t+\Delta t}, \bar{p}_{t+\Delta t}, \sigma_{f(t+\Delta t)}$ with the new decomposition. Check for convergence again, go back to step (2).
- (6) Repeat calculations for $\psi_{t+\Delta t}, \tau_{t+\Delta t}, \bar{p}_{t+\Delta t}, \sigma_{f(t+\Delta t)}$ with the new decomposition of $\mathbf{F}_{t+\Delta t}$ until the convergence $\tau_{t+\Delta t} + a\bar{p}_{t+\Delta t} - \sigma_{f(t+\Delta t)} \leq 0$ is reached.
- (7) Update the temperature $T(t + \Delta t)$ for next step similar to conventional staggered update algorithm for thermo-mechanical coupled problems.

4. Computational simulations and experimental validation

Two types of simulations are conducted with the ABAQUS commercial code, in which the BMG constitutive model are incorporated through the user material subroutine (UMAT). The first is a simple numerical simulation of a single material point that is assumed to lie inside a shear band. This numerical experiment is conducted to examine the effectiveness of the proposed model in comparison with that in [4]. The second is a three-dimensional finite element simulation for uniaxial-compression test. While 2-dimensional simulations has been conducted in the literature [5,14], the 3D model is used to better understand the 3D shear band formation process.

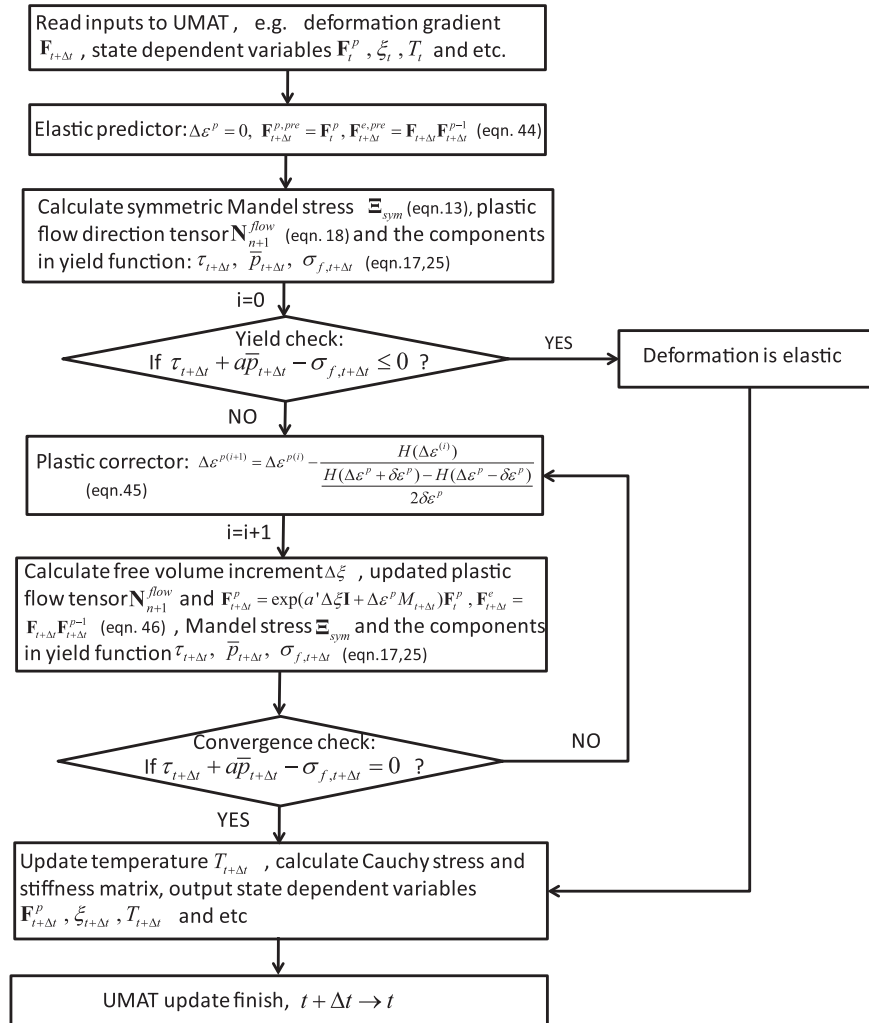


Fig. 1. Flow chart of the integration algorithm implemented in ABAQUS-UMAT.

4.1. Quasi-static compression behavior in various temperature and strain rate

In this example, a uniaxial compression simulation is performed to test the validity of the constitutive model and verify its numerical implementation through comparison with a similar study in [4]. The problem domain is setup by assuming a temperatures from 295 K to 687 K and strain-rates from 0.0001 to 0.32. The true stress–strain results from this simulation are small volume inside a shear band with an applied normal compression and shear load on the top and bottom surfaces respectively. Following the studies in [4,26,5], the tests are conducted for the BMG Vitreloy-1 over a range of compared with experiment data given in [1,18] and also with results from a 3D simulation of a single 8-noded brick element in ABAQUS, under the same loading conditions. The true stress–strain responses are shown in the Figs. 2–4, 6 and 7.

Fig. 2 shows the true stress–strain response for simulations conducted at a temperature of 295 K and compares it with experimental data in [1,18,27]. The experimental data in the figure are for a strain-rate of 1×10^{-4} . as there is no significant rate-effect observed at this temperature. This rate insensitivity, especially at smaller strains, is also reflected in the model predictions with almost overlapping responses. The drop in stress is due to the free-volume induced drop in viscosity as shown in Fig. 3, which depicts the non-Newtonian viscosity evolution for different strain-rates at

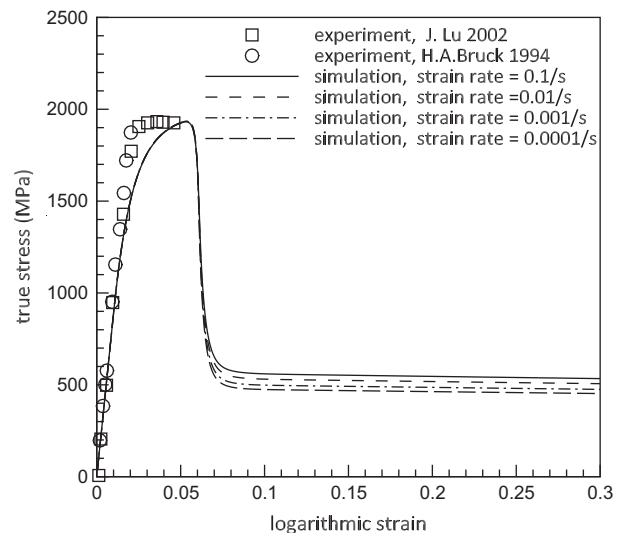


Fig. 2. True stress–strain response for various strain-rates (0.1, 0.01, 0.001, 0.0001) at 295 K in uniaxial compression simulations. Experimental data are taken from [1,18,27].

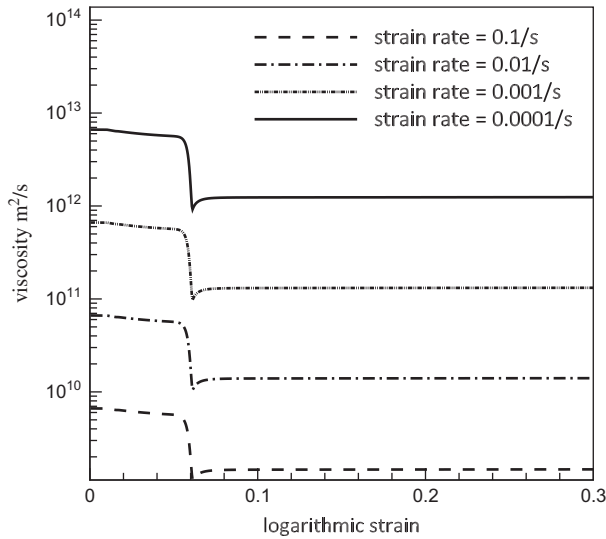


Fig. 3. Viscosity evolution for various strain-rates (0.1, 0.01, 0.001, 0.0001) at 295 K in uniaxial compression simulations.

295 K. Furthermore, strain-rate-dependent free-volume evolution is the only disordering mode, since as $c = 1$ in Eq. (38).

Fig. 4a–c presents the simulated stress–strain behavior of Vitreloy-1 in the vicinity of the glass transition temperature, i.e. at 613 K, 623 K and 643 K, for different applied strain-rates ranging from 1×10^{-5} to 0.32. In this regime, the power-density-dependent free-volume evolution part starts to dominate in Eq. (38), as c approaches 0. This is shown in Fig. 5 which illustrates the evolution of c with flow stress and temperature. The results show that the power-strain rate-dependent free-volume evolution model is able to match the experimental results well. The stress–strain response is highly strain-rate sensitive in this temperature range. It is noticed that for a temperature 613 K, there is a stress undershoot right after a stress drop and before reaching steady-state. This results from a free volume relaxation process, probably due to free volume diffusion, which is not captured by the simulation. Also for a temperature 623 K at an advanced deformation stage after reaching steady-state stress, different softening and hardening behaviors seem to appear. It is unclear what causes this behavior, and it only occurs in the experiments at a temperature 623 K. This is also not captured by simulation. At low strain rates e.g. at 2×10^{-4} , the peak stress is low and the strain softening phenomenon is nearly non-existent. This results in a homogeneous deformation. This result is also in contrast with Fig. 2, where shear band tends to form indicating nonhomogeneous deformation.

Fig. 6 presents the results of numerical simulations at 683 K, both under isothermal and adiabatic heating conditions. In the temperature evolution Eq. (43), the left hand side corresponds to the local change in thermal energy, the first term on right hand side is the heat source from plastic energy dissipation and the second term is the heat flux. Under isothermal conditions with $\dot{T} = 0$ in Eq. (43), the results agree rather well with experiments at relatively low strain-rates, e.g. from 1×10^{-1} /s to 1×10^{-2} /s. In this regime, the system has enough time to reach a thermal equilibrium state.

However, at a strain-rate of 3.2×10^{-1} /s, this model under quasi-static assumptions predicts a higher equilibrium stress than is experimentally observed, for higher strains. This may be caused by the temperature changes as within shear bands, representing adiabatic heating conditions. Consequently, adiabatic heating with the heat flux term $\nabla \cdot \mathbf{H} = 0$ in Eq. (43), and transient heat transfer must be taken into account in the numerical simulations in this

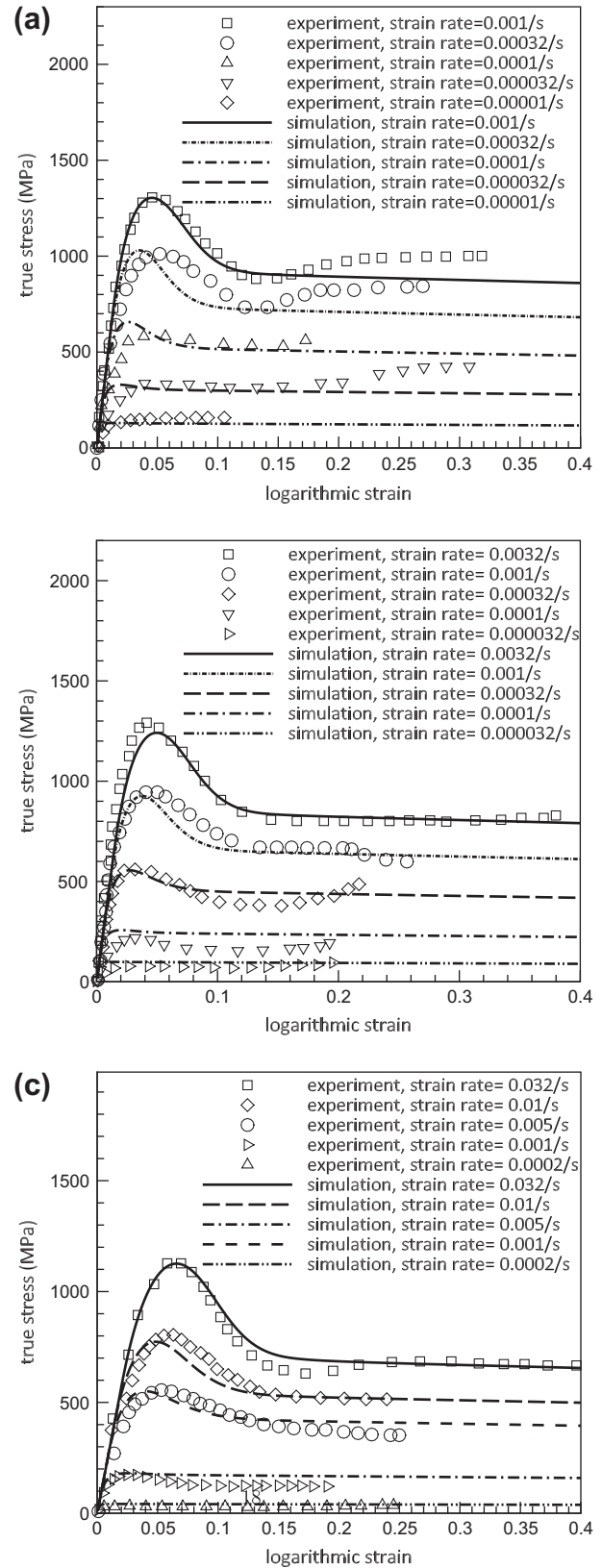


Fig. 4. True stress–strain response for various strain-rates at (a) 613 K, (b) 623 K, and (c) 643 K in uniaxial compression simulations. Experimental data are taken from [1,18].

temperature regime. Numerical simulations with adiabatic heating are conducted. For lower strain-rates ≤ 0.1 , the temperature rise

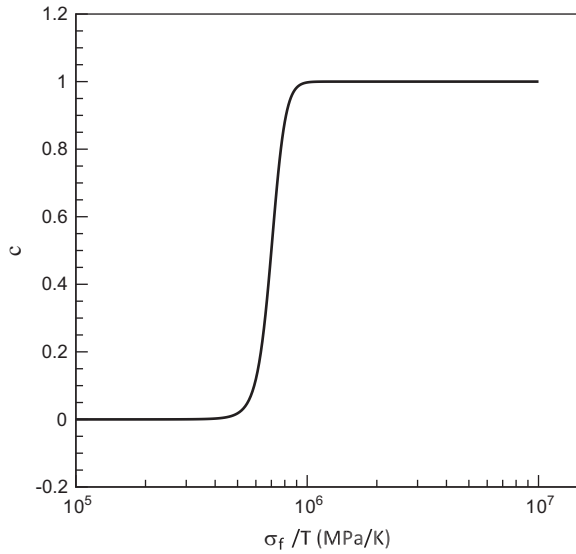


Fig. 5. The parameter c in the free-volume evolution law (38) as a function of flow stress and temperature.

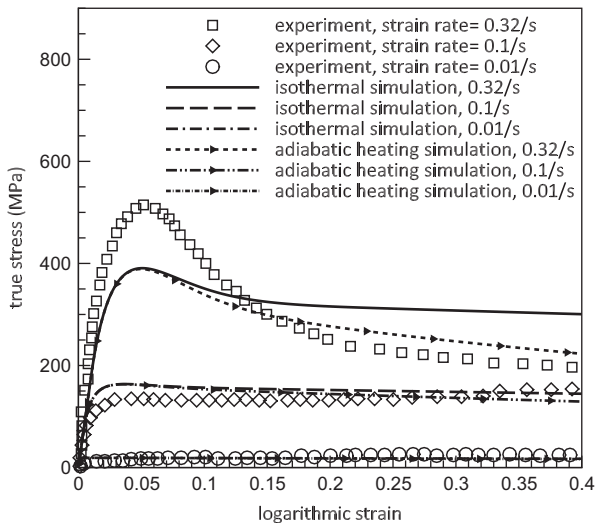


Fig. 6. True stress–strain response for various strain-rates at 683 K in uniaxial compression simulations. Experimental data are taken from [1,18].

due to plastic dissipation is very small and thus the isothermal and adiabatic heating conditions do not exhibit much difference. At higher rates, even including the adiabatic heating condition does not significantly improve the simulated results as seen in Fig. 6. The peak stress at lower strains is significantly lower in the model, however better match with the experimental results are observed at much higher strains beyond the plot in the figure.

4.1.1. Strain-rate jump test

In this example, numerical simulations are conducted with a jump in the strain-rate at a temperature of 643 K (near the glass transition temperature 625 K) corresponding to experiments in [1,18]. Initially the specimen is deformed at a strain-rate of $5 \times 10^{-3} \text{ s}^{-1}$. At 20% strain, the strain-rate is instantaneously increased to 1×10^{-2} , and again at 40% strain the strain-rate is reduced back to $5 \times 10^{-3} \text{ s}^{-1}$. The stress–strain response, simulated by a single C3D8 element in ABAQUS, is shown in Fig. 7. With the upward jump in the strain-rate, the stress level increases to a

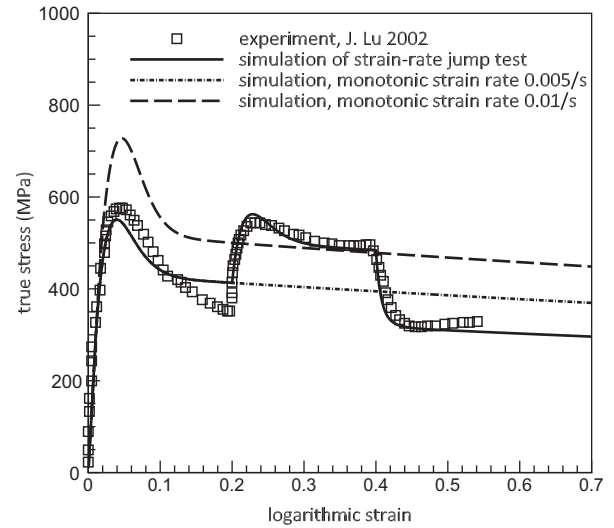


Fig. 7. True stress–strain response with instantaneous changes in the strain-rates at 643 K in uniaxial compression simulations. Experimental data are taken from [1,18].

new peak before strain-softening takes place again. Again with the drop in the strain-rate to $5 \times 10^{-3} \text{ s}^{-1}$, the stress peak drops below the steady-state response before slowly catching up again. The simulation results show that model captures the strain-rate dependence rather well at this temperature.

4.2. Micro-indentation simulations

Simulations of a spherical indentation tests of Vitreloy-1 is performed to study the hydrostatic pressure sensitivity and also to validate the proposed constitutive model for BMGs. The experiment data are taken from [8], in which a micro-indenter (Micro Hardness Tester, CSM instruments, Switzerland) is loaded in a force control mode at a load rate of 2 N/min. The indenter tip has a radius of $R = 50 \mu\text{m}$ that is significantly smaller than the BMG material specimen. The experimental temperature is around room temperature of $T = 295 \text{ K}$.

The simulation is performed using a plane-strain model in the ABAQUS code with 1000 (40×25) CPE4 full integration plane strain elements as shown in Fig. 8. The figure shows a converged mesh with respect to stress results. The ratio of the size of the specimen to the indenter tip radius in the model are: $\frac{H}{R} = 4$, $\frac{W}{R} = 8$. The contact between the rigid indenter tip and specimen is set to be frictionless, and the penalty method is used to enforce the non-penetration constraint. Displacement-control is applied at the reference point of the rigid tip with two rates, viz. $10 \mu\text{m/s}$ and $1 \mu\text{m/s}$ respectively. In this range of rates at room temperature, the BMG material is rate-insensitive, and displacement control used in the simulation should give the same results as under load-control applied in experiments.

The contour plot of the von-Mises stress is shown in Fig. 9 corresponding to a maximum indentation depth of $0.18R$. The specimen is large enough to avoid effects of boundaries other than the indenter. The maximum stress is around 1.9 GPa, which is consistent with the experimentally observed yield stress in [8]. The normalized displacement–load responses with different hydrostatic pressure sensitivity coefficients $a = 0.0, 0.045, 0.13, 0.2$ are plotted in Fig. 9. The displacement is normalized with the indenter radius as h/R and the load is normalized as P/ER^2 , where $E = 96 \text{ GB}$ is the elastic modulus. The pure elastic solution predicts the same slope as experiments in the elastic deformation regime, i.e. ($h/R < 0.1$). However, the inelastic portion of the deformation shows a much

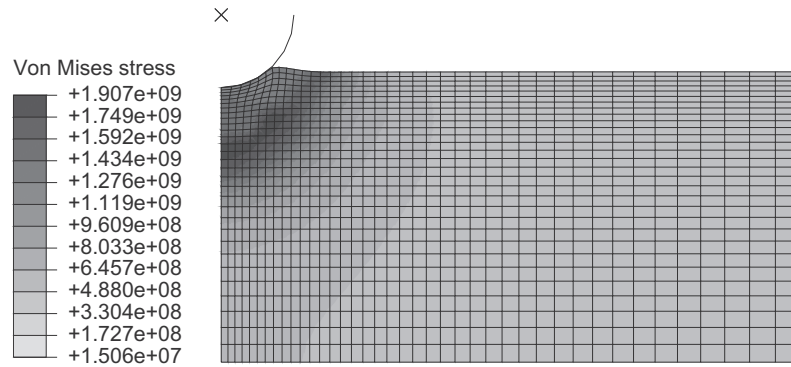


Fig. 8. Von-Mises stress contour plot at maximum indentation depth in the indentation example. Dimensions of the model correspond to $\frac{H}{R} = 4$, $\frac{W}{R} = 8$ where H and W correspond to the height and width of the specimen and R is the indenter tip radius.

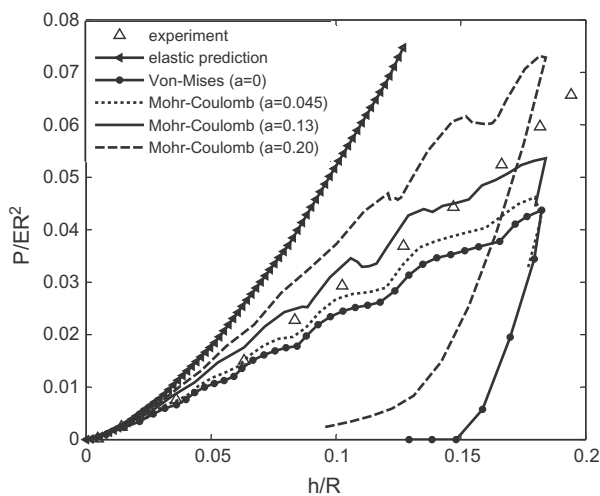


Fig. 9. Normalized load–displacement plots in the indentation test exhibiting results using pure elastic, non-linear with Mises yield function and non-linear with Mohr–Coulomb yield function. The triangular dots represent experimental data from [8].

higher slope. The stresses obtained by using the von Mises yield function with $a = 0.0$ in Eq. (17), have lower values than the experimental results. With increasing a in Eq. (17), the slopes of the simulated load–displacement plots increase, and at $a = 0.13$ it shows the best match with experimental data. This value is used in the compression tests to predict the stress–strain behavior.

No noticeable difference is observed at a constant a with different loading rates (not shown). This is consistent with the previous stress–strain results in compression tests at room temperature where the strain-rate dependence does not exist.

4.3. 3-D compression simulation showing shear band formation

The BMG model is further validated with a 3-D **uniaxial compression simulation** for the material $\text{Zr}_{50.7}\text{Cu}_{28}\text{Ni}_9\text{Al}_{12.3}$. The material properties have been given in [28] and include the glass transition temperature of 719 K, yield strength 1.9 GPa, heat capacity 12.9 kJ/mol. Fig. 10 shows half of a cylinder that is modeled using 21,318 8-noded brick elements with selective reduced integration in ABAQUS. Displacement boundary conditions are applied on the top and bottom surface nodes in vertical direction as the loading. Adiabatic heating condition is assumed for the simulations, with nodes on the top and bottom boundary set to a constant ambient temperature of 295 K as a temperature boundary

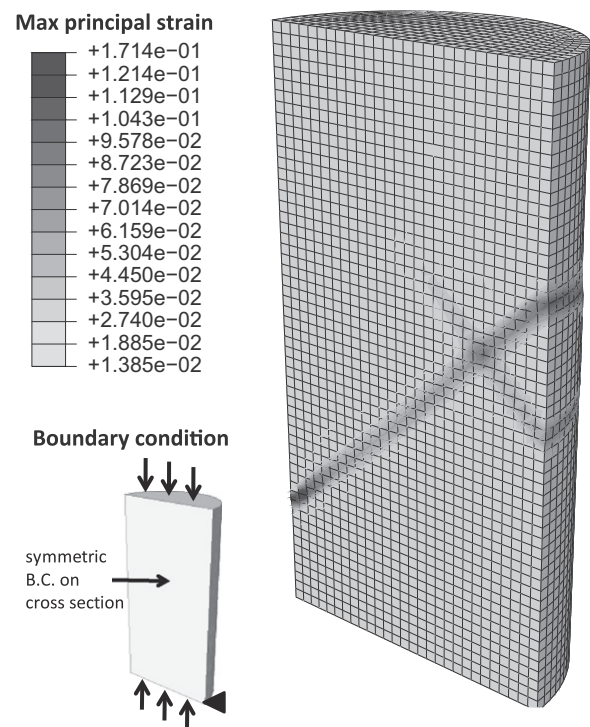


Fig. 10. The finite element model and mesh in ABAQUS showing the shear band and the principal strains.

condition. A weak point is introduced at a location inside the specimen to initiate a local stress concentration and trigger shear banding. At this point, the threshold stress σ_0 in Eq. (25) is set to a 20% lower value than other points in the body. Physically this corresponds to a local defect, such as precipitate or local free-volume concentration, for which the location is chosen in the way to represent the general case. The weak point is applied in a symmetric way so that only half the cylinder can be modeled. The principal strain distribution at 3.5% overall applied strain is plotted in the Fig. 10. The strain is highly localized in a thin shear-band plane across the specimen, which is the precursor to fracture.

Results of the simulation are presented in Fig. 11. The overall stress is calculated from the net vertical reaction force on the top and bottom surfaces respectively, while the overall strain corresponds to the applied displacement. The stress–strain response is plotted in Fig. 11a. In the initial stages of elastic deformation (point A in Fig. 11) at a uniform rate over the whole body, the deformation

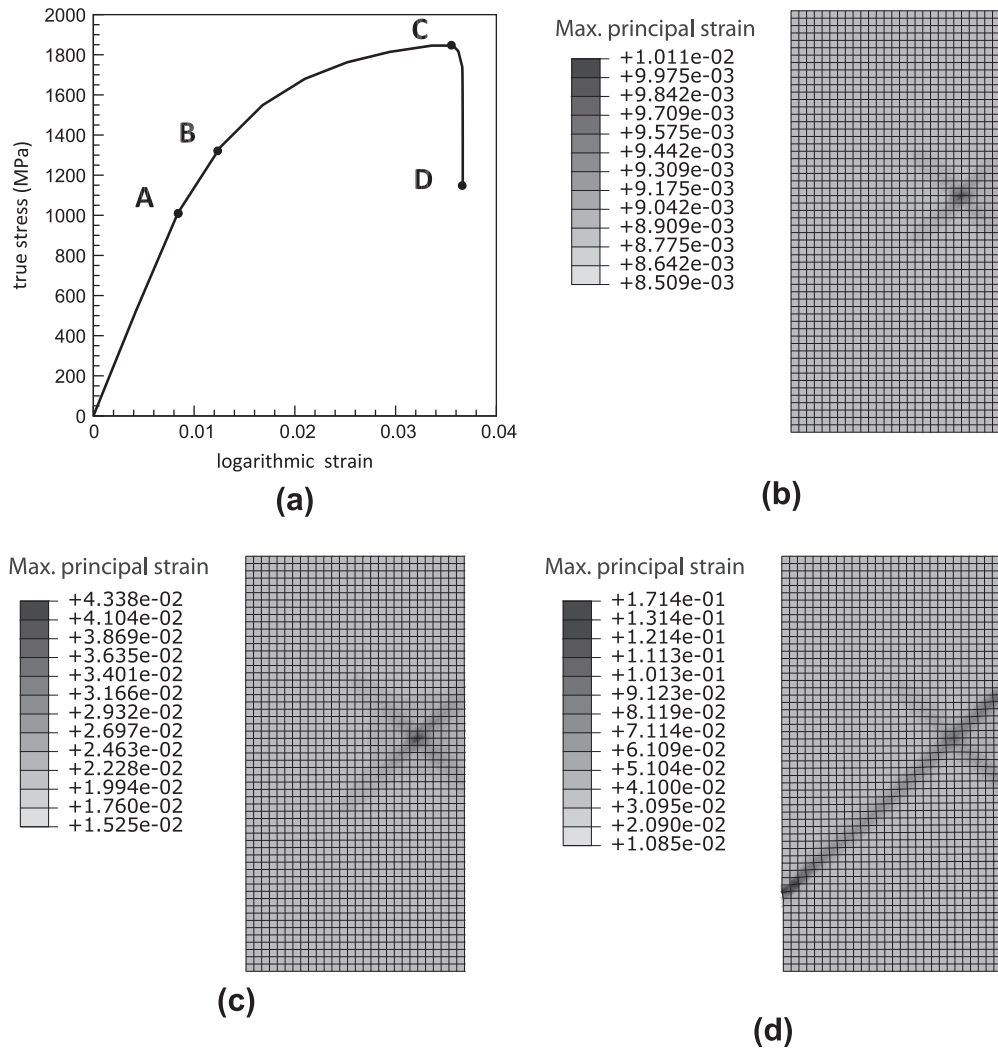


Fig. 11. Progression of deformation in a cylindrical BMG (2D section through the center) showing the formation of a shear band formation: (a) stress–strain response during the compression test; (b) principal strain contour at initiation of strain localization in the shear band; (c) principal strain contour before the sudden growth of shear band; and (d) principal strain contour after the shear band go through entire body and strain localized in shear band.

is homogeneous. (b). Next, plastic deformation is initiated at the weak point, which start to lead to strain localization and stress concentration in this region as shown in Fig. 11b. The shear plane is initiated at this point (point B in Fig. 11) and will grows in the direction of plastic flow. Near the stress concentration region, the plastic strain accumulates faster than other regions. With this high plastic shear-rate, the local free-volume increase much faster and leads to a drop in viscosity, resulting in material softening (point C in Fig. 11). As a consequence the strain and strain-rate further increase in this “soft” shear plane and intensify this process. Finally the shear plane go through the entire body inside which the strain and strain rate highly localized as shown in Fig. 11c and d. This simulation result is consistent with the experimental observations described in [28].

This example also provides a method for studying pressure sensitivity, by measuring the inclination angle of the shear band with respect to the axes of the cylinder. An analytical form of the orientation of the fracture surface (usually the same location as the shear band) is given in [6] in terms of the hydrostatic pressure in the yield function by referring to the Mohr’s circle. The inclination angles in a variety of BMG’s for room temperature compression tests have been summarized in [9] and given in Table 2. The simulations using a value $a = 1.3$ in Eq. (17) yield an inclination of 43°

Table 2

Reported inclination angles of shear band in uniaxial compression tests.

Ref.	BMG classification	Fracture angle (θ_c)
Donovan [29]	Pd ₄₀ Ni ₄₀ P ₂₀	$\theta_c = 41.9 \pm 1.2^\circ$
Lowhaphandu et al. [30]	Zr ₆₂ Ti ₁₀ Ni ₁₀ Cu _{14.5} Be _{3.5}	$\theta_c = 41.6 \pm 2.1^\circ$
Wright et al. [31]	Zr ₄₀ Ti ₁₄ Ni ₁₀ Cu ₁₂ Be ₂₄	$\theta_c = 42^\circ$
He et al. [32]	Zr _{52.5} Ni _{14.6} Al ₁₀ Cu _{17.9} Ti ₅	$\theta_c = 40\text{--}45^\circ$
Zhang et al. [9]	Zr ₅₉ Cu ₂₀ Al ₁₀ Ni ₈ Ti ₃	$\theta_c = 43^\circ$

(see Fig. 12). This is within acceptable tolerance of the values in the Table 2.

5. Conclusions

Bulk metallic glasses exhibit different mechanical behavior, such as strain-rate sensitivity and softening, over a range of temperatures from room temperature to over the glass transition temperature. Strain-rate insensitive and inhomogeneous deformation with the formation of shear band is observed at room temperature, while a transition from Newtonian flow to non-Newtonian flow, inhomogeneous to homogeneous deformation is observed around glass transition temperatures. This paper develops a free-volume

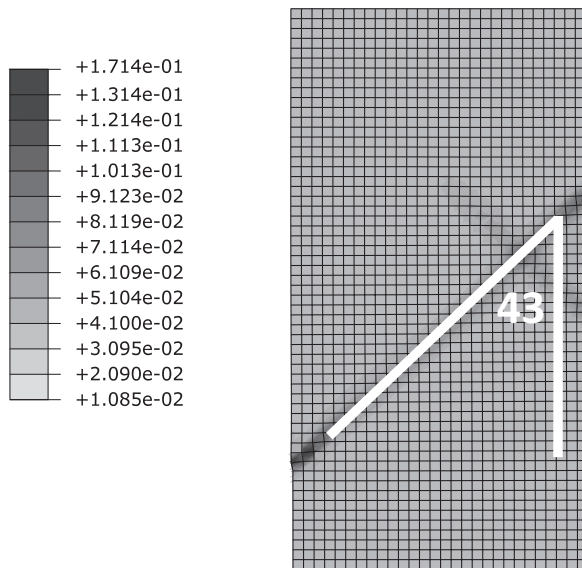


Fig. 12. The shear band inclination angle in the deformed cylinder.

theory based constitutive model to capture the different deformation mechanisms over this temperature range. Inspired by the free-volume theory in [2], a mixed power-density and strain-rate-dependent free volume kinetic law is proposed, which describes the transition of free volume evolution from that dominated by the stress power to one dominated by strain-rate with temperature change. The logarithmic strain and the thermodynamically driven Mandel stress are adopted as primary variables, which results in the time-integration following a relatively simple small-strain type update process. This model, using a Mohr–Coulomb type yield function, is capable of effectively describing finite deformation with localization in shear bands. A series of numerical simulations are conducted with this model, both for uniaxial and three-dimensional problems, and compared with experimental results. The stress–strain response predicted by this model near the glass transition temperature matches well with the uniaxial compression test results, as well as with the strain-rate jump test results. The simulation results suggest that material softening and inhomogeneous deformation result from the decrease in viscosity caused by an increase in free-volume. The Mohr–Coulomb yield function based model also captures the results of indentation tests at room temperature. Another important aspect is the formation of shear bands, which usually lead to failure. Three-dimensional simulations with this model implemented in ABAQUS, illustrate the formation process of the shear band in uniaxial compression tests. The study of shear band inclination angles further validates the hydrostatic stress dependence in the yield criteria adopted in this model. In conclusion, the paper

demonstrates that the constitutive framework incorporating finite deformation kinematics, the Mohr–Coulomb yield criteria and the kinetic law governing the evolution of density and free volume under different strain rates is able to accurately represent the macroscopic behavior for bulk metallic glasses for a certain range of temperatures and strain rates. Better representation of the behavior can be achieved through the incorporation multi-scale models for BMGs and that will be the subject of a future paper.

Acknowledgments

This work has been supported by the Air Force Office of Scientific through a grant (AFOSR Grant #FA9550-09-1-0251, Program Manager: Dr. Ali Sayir) with Dr. K. Flores as the lead PI. This sponsorship is gratefully acknowledged.

References

- [1] J. Lu, Mechanical Behavior of a Bulk Metallic Glass and its Composite Over a Wide Range of Strain Rates and Temperatures, PhD thesis, California Institute of Technology, 2002.
- [2] F. Spaepen, *Acta Metall.* 25 (1977) 407–415.
- [3] A.S. Argon, *Acta Mater* 27 (1979) 47–58.
- [4] Q. Yang, A. Mota, M. Ortiz, *Comput. Mech.* 37 (2006) 194–204.
- [5] P. Thamburaja, R. Ekambaram, *J. Mech. Phys. Solids* 55 (2007) 1236–1273.
- [6] M. Zhao, M. Li, *Appl. Phys. Lett.* 93 (2008) 241906.
- [7] R. Vaidyanathan, G. Ravichandran, M. Dao, S. Suresh, *Acta Mater.* 49 (2001) 3781–3789.
- [8] M.N.M. Patnaik, R. Narasimhan, U. Ramamurty, *Acta Mater.* 52 (2004) 3335–3345.
- [9] Z.F. Zhang, J. Eckert, L. Schultz, *Acta Mater.* 51 (2003) 1167–1179.
- [10] M. Heggen, F. Spaepen, M. Feuerbacher, *J. Appl. Phys.* 97 (2005) 033506.
- [11] F.J. Montans, K.J. Bathe, *Comput. Plast.* 7 (2007) 13–36.
- [12] M.A. Caminero, F.J. Montans, K.J. Bathe, *Comput. Struct.* 89 (2011) 826–843.
- [13] F.J. Montans, K.J. Bathe, *Int. J. Numer. Methods Eng.* 63 (2005) 159–196.
- [14] M. Zhao, *J. Mater. Res.* 24 (2009) 2688–2696.
- [15] R. Bhowmick, R. Raghavan, K. Chattopadhyay, U. Ramamurty, *Acta Mater.* 54 (2006) 4221–4228.
- [16] M. Ortiz, L. Stainier, *Comput. Meth. Appl. Mech. Eng.* 171 (1999) 419–444.
- [17] A. Masuhr, T.A. Waniuk, R. Busch, W.L. Johnson, *Phys. Rev. Lett.* 82 (1999) 2290–2293.
- [18] J. Lu, G. Ravichandran, W.L. Johnson, *Acta Mater.* 51 (2003) 3429–3443.
- [19] P. de Hey, J. Sietsma, A. Van Den Beukel, *Acta Mater.* 46 (1998) 5873–5882.
- [20] G.S. Grest, M.H. Cohen, *Adv. Chem. Phys.* 48 (1981) 455–525.
- [21] P. Yu, R.J. Wang, D.Q. Zhao, H.Y. Baia, *Appl. Phys. Lett.* 90 (2007) 251904.
- [22] Y.Q. Cheng, E. Ma, *Phys. Rev. B* 80 (2009) 064104.
- [23] Z. Zhang, V. Keppens, T. Egami, *J. Appl. Phys.* 102 (2007) 123508.
- [24] R.B. Dupaix, M.C. Boyce, *Mech. Mater.* 39 (2007) 39–52.
- [25] J.C. Simo, T.J.R. Hughes, *Computational Inelasticity*, in: *Interdisciplinary Applied Mathematics Series*, first ed., Springer, 1998.
- [26] Q. Yang, *Thermomechanical Variational Principles for Dissipative Materials with Application to Strain Localization in Bulk Metallic Glasses*, PhD thesis, California Institute of Technology, 2004.
- [27] H.A. Bruck, T. Christman, A.J. Rosakis, W.L. Johnson, *Scripta Mater.* 30 (1994) 429–434.
- [28] W. Zheng, Y.J. Huang, G.Y. Wang, P.K. Liaw, J. Shen, *Metall. Mater. Trans. A* 42A (2011) 1491–1498.
- [29] P.E. Donovan, *Mater. Sci. Eng.* 98 (1988) 487.
- [30] P. Lowhaphandu, S.L. Montgomery, J.J. Lewandowski, *Scripta Mater.* 41 (1999) 19–24.
- [31] W.J. Wright, R. Saha, W.D. Nix, *Mater. Trans. JIM.* 42 (2011) 642–649.
- [32] G. He, J. Lu, Z. Bian, D. Chen, G. Chen, G. Tu, G. Chen, *Mater. Trans. JIM.* 42 (2011) 356–364.